

# Saturation-Aware Snapshot Compressive Imaging: Theory and Algorithm

Mengyu Zhao\*, Shirin Jalali\*

## Abstract

Snapshot Compressive Imaging (SCI) uses coded masks to compress a 3D data cube into a single 2D snapshot. In practice, multiplexing can push intensities beyond the sensor’s dynamic range, producing saturation that violates the linear SCI model and degrades reconstruction. This paper provides the first theoretical characterization of SCI recovery under saturation. We model clipping as an element-wise nonlinearity and derive a finite-sample recovery bound for compression-based SCI that links reconstruction error to mask density and the extent of saturation. The analysis yields a clear design rule: optimal Bernoulli masks use densities below one-half, decreasing further as saturation strengthens. Guided by this principle, we optimize mask patterns and introduce a novel reconstruction framework, *Saturation-Aware PnP Net (SAPnet)*, which explicitly enforces consistency with saturated measurements. Experiments on standard video-SCI benchmarks confirm our theory and demonstrate that SAPnet significantly outperforms existing PnP-based methods.

## 1 Introduction

Snapshot compressive imaging (SCI) enables fast acquisition of high-dimensional 3D data cubes, such as video [1] and hyperspectral images [2, 3], via specialized optical encoding that maps a 3D data cube into a single 2D snapshot [4]. A critical issue in SCI is sensor saturation, which is more prevalent than in conventional imaging because multiple frames are multiplexed into a single exposure. When the summed intensities exceed the detector’s full-well capacity or analog-to-digital converter (ADC) range, the readout clips (saturates), introducing a nonlinearity that violates the linear SCI model and biases downstream reconstructions, typically causing loss of detail in bright regions and structured artifacts.

Saturation and clipping have been studied in compressed sensing under various nonlinearities, including saturation rejection and consistency methods [5, 6], presaturation errors with noise [7, 8], and quantization effects. However, these analyses apply to generic compressed sensing rather than SCI. In SCI, most prior efforts mitigate saturation empirically, e.g., by designing adaptive or trainable masks [9–14], incorporating PSF preprocessing to reduce clipping [15]. These works optimize optics or networks but lack recovery guarantees. Despite broad recognition of saturation [15–17], a theory that explicitly models it within SCI remains absent; existing analyses assume a linear, unsaturated forward model [18, 19]. This gap motivates our development of a theory for SCI under saturation that clarifies how optical encoding (e.g., mask density) and saturation severity jointly govern reconstruction accuracy.

**Contributions.** We adopt the compression-based SCI recovery framework that is standard in theoretical analyses [18, 19] and develop, to our knowledge, the first theory of SCI under saturation. Specifically: (i) we model clipping as an element-wise nonlinearity and derive a finite-sample recovery bound for compression-based SCI; (ii) the bound makes explicit how reconstruction error depends on mask density and the severity of saturation, yielding a simple mask-design rule; (iii) we instantiate this rule by optimizing Bernoulli mask patterns and pairing them with a new saturation-aware plug-and-play (PnP) reconstruction method; and (iv) experiments on standard video-SCI benchmarks validate the analysis, largely improving robustness and

---

\*Rutgers University, New Brunswick, Department of Electrical and Computer Engineering (mengyu.zhao@rutgers.edu, shirin.jalali@rutgers.edu).

accuracy over conventional masks. Together, these results deepen understanding of saturation in SCI and enable more informed optical and algorithmic design.

**Notations.** Vectors are represented using bold characters, such as  $\mathbf{x}$  and  $\mathbf{y}$ . For a matrix  $\mathbf{X} \in \mathbb{R}^{n_1 \times n_2}$ ,  $\text{Vec}(\mathbf{X}) \in \mathbb{R}^n$  denotes its vectorized form, where  $n = n_1 n_2$ , constructed by concatenating the columns of  $\mathbf{X}$ . For  $\mathbf{A}, \mathbf{B} \in \mathbb{R}^{n_1 \times n_2}$ , the Hadamard product  $\mathbf{Y} = \mathbf{A} \odot \mathbf{B}$  is defined element-wise such that  $Y_{ij} = A_{ij} B_{ij}$ . Sets are denoted by calligraphic letters, such as  $\mathcal{A}$  and  $\mathcal{B}$ . For a finite set  $\mathcal{A}$ ,  $|\mathcal{A}|$  indicates its cardinality.  $(\cdot)_+$  operator represents  $\max(\cdot, 0)$ .

## 2 Problem statement

**Linear SCI forward model.** Let  $\mathbf{X} \in \mathbb{R}^{n_1 \times n_2 \times B}$  be the target cube and  $\mathbf{Y} \in \mathbb{R}^{n_1 \times n_2}$  the snapshot. With masks  $\mathbf{C} = \{\mathbf{C}_b\}_{b=1}^B$ , the standard SCI model is

$$\mathbf{Y} = \sum_{b=1}^B \mathbf{C}_b \odot \mathbf{X}_b + \mathbf{Z},$$

where  $\mathbf{Z}$  is additive noise and  $\odot$  denotes element-wise product. Vectorizing  $\mathbf{x}_b = \text{vec}(\mathbf{X}_b) \in \mathbb{R}^n$  ( $n = n_1 n_2$ ), stack  $\mathbf{x} = [\mathbf{x}_1^\top, \dots, \mathbf{x}_B^\top]^\top \in \mathbb{R}^{nB}$  and define  $\mathbf{y} = \text{vec}(\mathbf{Y})$ ,  $\mathbf{z} = \text{vec}(\mathbf{Z})$ . Then

$$\mathbf{y} = \mathbf{H}\mathbf{x} + \mathbf{z}, \quad \mathbf{H} = [\mathbf{D}_1 \cdots \mathbf{D}_B], \quad (1)$$

where for  $b = 1, \dots, B$ ,  $\mathbf{D}_b = \text{diag}(D_{b1}, \dots, D_{bn}) = \text{diag}(\text{vec}(\mathbf{C}_b))$ . The goal of the SCI recovery algorithm is to reconstruct  $\mathbf{x} \in \mathbb{R}^{nB}$  from  $\mathbf{y} \in \mathbb{R}^n$  given  $\mathbf{H}$ .

**Clipping (saturation) nonlinearity.** We model saturation via element-wise clipping at threshold  $T > 0$ :

$$\mathbf{y}_T = \text{clip}(\mathbf{y}; T), \quad [\text{clip}(\mathbf{u}; T)]_i = \min\{u_i, T\}.$$

(If negatives are possible, one may use  $[\text{clip}(\mathbf{u}; 0, T)]_i = \min\{\max\{u_i, 0\}, T\}$ ; our analysis uses the nonnegative form above.) Note that for binary masks and signals satisfying  $\|\mathbf{x}\|_\infty \leq \rho/2$ ,  $y_i = \sum_{b=1}^B D_{b,i} x_{b,i} \leq B\rho/2$ . Therefore, for  $T \geq B\rho/2$ ,  $\text{clip}(\mathbf{y}; T) = \mathbf{y}$ , which implies no saturation for all inputs.

**Compression-based SCI recovery.** We adopt the compression-based recovery framework common in SCI theory [18, 19]. Let  $\mathcal{Q} \subset \mathbb{R}^{nB}$  denote a compact signal class. A rate- $r$  compression code  $(f, g)$  induces a codebook  $\mathcal{C} = \{g(f(\mathbf{x})) : \mathbf{x} \in \mathcal{Q}\}$  with  $|\mathcal{C}| \leq 2^{Br}$  and worst-case distortion  $\delta = \sup_{\mathbf{x} \in \mathcal{Q}} \frac{1}{nB} \|\mathbf{x} - g(f(\mathbf{x}))\|_2^2$ . The compression-based estimator (CSP) solves  $\hat{\mathbf{x}} \in \arg \min_{\mathbf{c} \in \mathcal{C}} \|\mathbf{y} - \mathbf{H}\mathbf{c}\|_2^2$ , as in [18, 19].

$$\hat{\mathbf{x}} \in \arg \min_{\mathbf{c} \in \mathcal{C}} \|\mathbf{y} - \mathbf{H}\mathbf{c}\|_2^2, \quad (2)$$

In the saturated setting we observe  $\mathbf{y}_T = \text{clip}(\mathbf{H}\mathbf{x} + \mathbf{z}; T)$ . Let  $\mathbf{y} = \mathbf{H}\mathbf{x} + \mathbf{z}$  and define the set of saturated measurement locations as

$$\mathcal{I}_s = \{j \mid y_j \geq T\}.$$

Given the saturated measurements  $\mathbf{y}_T$ , we modify the compression-based optimization (2) as follows

$$\hat{\mathbf{x}} = \arg \min_{\mathbf{c} \in \mathcal{C}} \left( \sum_{i \in \mathcal{I}_s} (y_{T,i} - (\mathbf{H}\mathbf{c})_i)^2 \mathbf{1}_{(\mathbf{H}\mathbf{c})_i \leq T} + \sum_{i \in \mathcal{I}_s^c} (y_{T,i} - (\mathbf{H}\mathbf{c})_i)^2 \right). \quad (3)$$

The central question is how saturation impacts recovery accuracy. In the next section, we characterize this effect by analyzing the performance of (3). Our results not only provide explicit recovery guarantees under clipping, but also reveal how mask density should be chosen to mitigate saturation-induced errors.

### 3 Recovery bounds for SCI under saturation

The recovery accuracy under saturation depends on the number of saturated measurements,  $|\mathcal{I}_s|$ . Since the masks  $\{D_{ij}\}$  are random, the size of  $\mathcal{I}_s$  is itself random. We therefore characterize saturation through the *expected fraction of saturated measurements*:

$$p_s(\mathbf{x}; T) \triangleq \frac{1}{n} \mathbb{E}[|\mathcal{I}_s|],$$

where the expectation is taken with respect to the mask distribution. Intuitively,  $p_s(\mathbf{x}; T)$  measures how often the SCI encoding pushes entries of  $\mathbf{H}\mathbf{x}$  beyond the sensor range.

The next result shows how this saturation probability directly enters the recovery bound for compression-based SCI, quantifying the additional error induced by clipping.

**Theorem 3.1** *Consider  $\mathcal{Q} \subset \mathbb{R}^{nB}$ , and assume that for all  $\mathbf{x} \in \mathcal{Q}$ ,  $\|\mathbf{x}\|_\infty \leq \rho/2$ . For  $\mathbf{x} \in \mathcal{Q}$ , let  $\mathbf{y}_T = \text{clip}(\sum_{i=1}^B \mathbf{D}_i \mathbf{x}_i + \mathbf{z}; T)$ , where  $z_i = 0$  for  $i \in \mathcal{I}_s$  and  $\|\mathbf{z}\|_2 \leq \epsilon_z$ , for some  $\epsilon_z \geq 0$ . Assume that the non-zero entries of the diagonal matrices  $\mathbf{D}_1, \dots, \mathbf{D}_B$  are drawn independently i.i.d.  $\text{Bern}(p)$ . Let  $\hat{\mathbf{x}}$  denote the solution of (3). Let  $\beta_T = (\frac{B\rho}{2} - T)^+$ . Then, given free parameters  $\epsilon_1, \epsilon_2 > 0$ , we have*

$$\begin{aligned} \frac{1}{\sqrt{nB}} \|\mathbf{x} - \hat{\mathbf{x}}\|_2 \leq & 2\sqrt{\frac{(1 - p_s(\mathbf{x}; T))}{nBp}} \epsilon_z + \\ & \sqrt{\left(1 + \frac{Bp}{1-p}\right)\delta + \frac{\rho^2 \epsilon_1}{p(1-p)} + (p_s(\mathbf{x}; T) + \epsilon_2)\beta_T \left(\frac{\beta_T}{B} + 4\rho\right)}. \end{aligned} \quad (4)$$

with probability larger than  $1 - 2^{Br+1} \exp(-\frac{n\epsilon_1^2}{2B^2}) - \exp(-2n\epsilon_2^2)$ .

The proof of Theorem 3.1 and its corollaries are provided in Section 4 of the extended version of our paper [20].

In the absence of saturation, we have  $p_s(\mathbf{x}; T) = 0$ , and Theorem 3.1 reduces to Theorem 1 in [21]. The first term in the bound in (4) reflects the impact of additive noise on the reconstruction error. The second term consists of two components, the latter quantifying the additional reconstruction error due to saturation. As the threshold  $T$  increases, the fraction of saturated measurements  $p_s(\mathbf{x}; T)$  and  $(\frac{B\rho}{2} - T)^+ ((\frac{B\rho}{2} - T)^+ + 4B\rho)$  both decrease. Consequently, the saturation error diminishes with larger  $T$ , and at  $T = \frac{B\rho}{2}$  this additional term vanishes entirely.

The following corollary highlights the mask-design implication of Theorem 3.1. For  $T > 0$ , let  $p_T^*$  denote the value of  $p$  that minimizes the recovery error bound in Theorem 3.1. The following corollary characterizes some of the properties  $p_T^*$ , which corresponds to the optimal mask distribution.

**Corollary 3.2** *Consider the same setup as in Theorem 3.1. Assume that  $\epsilon_z = 0$ . For any  $T > 0$ ,  $p_T^* < \frac{1}{2}$ . Furthermore,  $p_T^*$  is a increasing function of  $T$ .*

Corollary 3.2 states that similar to the case of saturation-free measurements, the optimal value of  $p_T^*$  always stays below 0.5 [19]. Furthermore, it states that as the saturation becomes more severe, to optimize the recovery performance, one needs to lower the density of non-zero entries in the masks.

## 4 Proofs

This section contains the proofs of the results stated in the previous section.

#### 4.1 Proof for Theorem 3.1

Let  $\tilde{\mathbf{x}} = g(f(\mathbf{x}))$ . By assumption, since  $\mathbf{x} \in \mathcal{Q}$ ,  $\|\mathbf{x} - \tilde{\mathbf{x}}\|_2^2 \leq nB\delta$ . When a small noise term  $\sigma_z$  is introduced in the non-saturated measurement process, let

$$\mathbf{y}_T = \text{clip}\left(\sum_{i=1}^B \mathbf{D}_i \mathbf{x}_i + \mathbf{z}\right), \quad \text{and} \quad \mathbf{y} = \sum_{i=1}^B \mathbf{D}_i \mathbf{x}_i + \mathbf{z},$$

denote the actual measurement vector and the ideal measurement vector, respectively. Since  $\hat{\mathbf{x}} = \arg \min_{\mathbf{c} \in \mathcal{C}} \left( \sum_{j \in \mathcal{I}_s} (y_{T,j} - (\mathbf{H}\mathbf{c})_j)^2 \mathbb{1}_{(\mathbf{H}\mathbf{c})_j \leq T} + \sum_{j \in \mathcal{I}_s^c} (y_{T,j} - (\mathbf{H}\mathbf{c})_j)^2 \right)$ , and  $\tilde{\mathbf{x}} \in \mathcal{C}$ , it follows that

$$\left( \sum_{j \in \mathcal{I}_s} (y_{T,j} - (\mathbf{H}\hat{\mathbf{x}})_j)^2 \mathbb{1}_{(\mathbf{H}\hat{\mathbf{x}})_j \leq T} + \sum_{j \in \mathcal{I}_s^c} (y_{T,j} - (\mathbf{H}\hat{\mathbf{x}})_j)^2 \right) \left( \sum_{j \in \mathcal{I}_s} (y_{T,j} - (\mathbf{H}\tilde{\mathbf{x}})_j)^2 \mathbb{1}_{(\mathbf{H}\tilde{\mathbf{x}})_j \leq T} + \sum_{j \in \mathcal{I}_s^c} (y_{T,j} - (\mathbf{H}\tilde{\mathbf{x}})_j)^2 \right). \quad (5)$$

Therefore,

$$\begin{aligned} & \sum_{j \in \mathcal{I}_s} \left( T - \sum_{i=1}^B D_{ij} \hat{x}_{ij} \right)^2 \mathbb{1}_{\sum_{i=1}^B D_{ij} \hat{x}_{ij} \leq T} + \sum_{j \in \mathcal{I}_s^c} \left( \sum_{i=1}^B D_{ij} (x_{ij} - \hat{x}_{ij}) + z_j \right)^2 \\ & \leq \sum_{j \in \mathcal{I}_s} \left( T - \sum_{i=1}^B D_{ij} \tilde{x}_{ij} \right)^2 \mathbb{1}_{\sum_{i=1}^B D_{ij} \tilde{x}_{ij} \leq T} + \sum_{j \in \mathcal{I}_s^c} \left( \sum_{i=1}^B D_{ij} (x_{ij} - \tilde{x}_{ij}) + z_j \right)^2 \end{aligned} \quad (6)$$

We next use the triangle inequality. Specifically, we have

$$\sqrt{\sum_{j \in \mathcal{I}_s^c} \left( \sum_{i=1}^B D_{ij} (x_{ij} - \hat{x}_{ij}) + z_j \right)^2} \geq \sqrt{\sum_{j \in \mathcal{I}_s^c} \left( \sum_{i=1}^B D_{ij} (x_{ij} - \hat{x}_{ij}) \right)^2} - \sqrt{\sum_{j \in \mathcal{I}_s^c} z_j^2}$$

and

$$\sqrt{\sum_{j \in \mathcal{I}_s^c} \left( \sum_{i=1}^B D_{ij} (x_{ij} - \hat{x}_{ij}) + z_j \right)^2} \leq \sqrt{\sum_{j \in \mathcal{I}_s^c} \left( \sum_{i=1}^B D_{ij} (x_{ij} - \hat{x}_{ij}) \right)^2} + \sqrt{\sum_{j \in \mathcal{I}_s^c} z_j^2}.$$

Then, we have

$$\begin{aligned} & \sqrt{\sum_{j \in \mathcal{I}_s} \left( T - \sum_{i=1}^B D_{ij} \hat{x}_{ij} \right)^2 \mathbb{1}_{\sum_{i=1}^B D_{ij} \hat{x}_{ij} \leq T} + \sum_{j \in \mathcal{I}_s^c} \left( \sum_{i=1}^B D_{ij} (x_{ij} - \hat{x}_{ij}) \right)^2} \\ & \leq \sqrt{\sum_{j \in \mathcal{I}_s} \left( T - \sum_{i=1}^B D_{ij} \tilde{x}_{ij} \right)^2 \mathbb{1}_{\sum_{i=1}^B D_{ij} \tilde{x}_{ij} \leq T} + \sum_{j \in \mathcal{I}_s^c} \left( \sum_{i=1}^B D_{ij} (x_{ij} - \tilde{x}_{ij}) \right)^2} + 2 \sqrt{\sum_{j \in \mathcal{I}_s^c} z_j^2} \end{aligned} \quad (7)$$

Let  $U = \sum_{j \in \mathcal{I}_s} (T - \sum_i D_{ij} \tilde{x}_{ij})^2 \mathbb{1}_{\sum_{i=1}^B D_{ij} \tilde{x}_{ij} \leq T} + \sum_{j \in \mathcal{I}_s^c} (\sum_{i=1}^B D_{ij} (x_{ij} - \tilde{x}_{ij}))^2$ . Then,

$$\begin{aligned}
U &= \sum_{j \in \mathcal{I}_s} (y_{T,j} - y_j + y_j - \sum_{i=1}^B D_{ij} \tilde{x}_{ij})^2 \mathbb{1}_{\sum_{i=1}^B D_{ij} \tilde{x}_{ij} \leq T} + \sum_{j \in \mathcal{I}_s^c} (\sum_{i=1}^B D_{ij} (x_{ij} - \tilde{x}_{ij}))^2 \\
&\stackrel{(a)}{\leq} |\mathcal{I}_s| \left( \frac{B\rho}{2} - T \right)^2 + 2 \sum_{j \in \mathcal{I}_s} (y_{T,j} - y_j) \left( y_j - \sum_{i=1}^B D_{ij} \tilde{x}_{ij} \right) \\
&\quad + \sum_{j \in \mathcal{I}_s} \left( \sum_{i=1}^B D_{ij} (x_{ij} - \tilde{x}_{ij}) \right)^2 + \sum_{j \in \mathcal{I}_s^c} \left( \sum_{i=1}^B D_{ij} (x_{ij} - \tilde{x}_{ij}) + z_j \right)^2 \\
&\leq |\mathcal{I}_s| \left( \frac{B\rho}{2} - T \right)^2 + 2 \sum_{j \in \mathcal{I}_s} |y_{T,j} - y_j| |y_j - \sum_{i=1}^B D_{ij} \tilde{x}_{ij}| + \left\| \sum_{i=1}^B \mathbf{D}_i (\mathbf{x}_i - \tilde{\mathbf{x}}_i) \right\|^2 \\
&\stackrel{(b)}{\leq} |\mathcal{I}_s| \left( \frac{B\rho}{2} - T \right)^+ \left( \left( \frac{B\rho}{2} - T \right)^+ + 2B\rho \right) + \left\| \sum_{i=1}^B \mathbf{D}_i (\mathbf{x}_i - \tilde{\mathbf{x}}_i) \right\|^2,
\end{aligned}$$

where (a) and (b) follow because for  $\mathbb{1}_{\mathcal{S}} \leq 1$ , for all  $\mathcal{S}$ , also for  $j \in \mathcal{I}_s$ ,  $|y_{T,j} - y_j| \leq (\frac{B\rho}{2} - T)^+$  and  $|y_j - \sum_{i=1}^B D_{ij} \tilde{x}_{ij}| \leq B\rho$ , respectively.

Similarly, let  $L = \sum_{j \in \mathcal{I}_s} (T - \sum_{i=1}^B D_{ij} \hat{x}_{ij})^2 \mathbb{1}_{\sum_{i=1}^B D_{ij} \hat{x}_{ij} \leq T} + \sum_{j \in \mathcal{I}_s^c} (\sum_{i=1}^B D_{ij} (x_{ij} - \hat{x}_{ij}))^2$ . Then,

$$\begin{aligned}
L &= \sum_{j \in \mathcal{I}_s} (y_{T,j} - y_j + y_j - \sum_{i=1}^B D_{ij} \hat{x}_{ij}) \mathbb{1}_{\sum_{i=1}^B D_{ij} \hat{x}_{ij} \leq T} + \sum_{j \in \mathcal{I}_s^c} (\sum_{i=1}^B D_{ij} (x_{ij} - \hat{x}_{ij}))^2 \\
&\geq -2 \sum_{j \in \mathcal{I}_s} |y_{T,j} - y_j| |y_j - \sum_{i=1}^B D_{ij} \hat{x}_{ij}| + \left\| \sum_{i=1}^B \mathbf{D}_i (\mathbf{x}_i - \hat{\mathbf{x}}_i) \right\|^2 \\
&\geq -2|\mathcal{I}_s| \left( \frac{B\rho}{2} - T \right)^+ B\rho + \left\| \sum_{i=1}^B \mathbf{D}_i (\mathbf{x}_i - \hat{\mathbf{x}}_i) \right\|^2. \tag{8}
\end{aligned}$$

Since from (6),  $L \leq U$ , combining (7), (8) and (8), it follows that

$$\left\| \sum_{i=1}^B \mathbf{D}_i (\mathbf{x}_i - \hat{\mathbf{x}}_i) \right\| \leq \sqrt{\left\| \sum_{i=1}^B \mathbf{D}_i (\mathbf{x}_i - \tilde{\mathbf{x}}_i) \right\|^2 + |\mathcal{I}_s| \left( \frac{B\rho}{2} - T \right)^+ \left( \left( \frac{B\rho}{2} - T \right)^+ + 4B\rho \right)} + 2\sqrt{\frac{n - |\mathcal{I}_s|}{n}} \epsilon_z. \tag{9}$$

Follow the similar steps in [19], and  $\mathbb{E}[|\mathcal{I}_s|] = np_s(\mathbf{x}; T)$  we have

$$\frac{1}{\sqrt{nB}} \|\mathbf{x} - \hat{\mathbf{x}}\|_2 \leq 2\sqrt{\frac{(1 - p_s(\mathbf{x}; T))}{nBp}} \epsilon_z + \sqrt{\left( 1 + \frac{Bp}{1-p} \right) \delta + \frac{\rho^2 \epsilon_1}{p(1-p)} + \frac{(p_s(\mathbf{x}; T) + \epsilon_2) \left( \frac{B\rho}{2} - T \right)^+ \left( \frac{B\rho}{2} - T \right)^+ + 4B\rho}{B}}. \tag{10}$$

Given  $\epsilon_1 > 0$  and  $\epsilon_2 > 0$  define events  $\mathcal{E}_1$ ,  $\mathcal{E}_2$  and  $\mathcal{E}_s$  as

$$\mathcal{E}_1 = \left\{ \frac{1}{n} \left\| \sum_{i=1}^B \mathbf{D}_i (\mathbf{x}_i - \tilde{\mathbf{x}}_i) \right\|_2^2 \leq \frac{p^2}{n} \left\| \sum_{i=1}^B (\mathbf{x}_i - \tilde{\mathbf{x}}_i) \right\|_2^2 + \frac{p-p^2}{n} \|\mathbf{x} - \tilde{\mathbf{x}}\|_2^2 + B\rho^2 \epsilon_1 / 2 \right\}, \tag{11}$$

$$\mathcal{E}_2 = \left\{ \frac{1}{n} \left\| \sum_{i=1}^B \mathbf{D}_i (\mathbf{x}_i - \mathbf{c}_i) \right\|_2^2 \geq \frac{p^2}{n} \left\| \sum_{i=1}^B (\mathbf{x}_i - \mathbf{c}_i) \right\|_2^2 + \frac{p-p^2}{n} \|\mathbf{x} - \mathbf{c}\|_2^2 - B\rho^2 \epsilon_1 / 2 : \forall \mathbf{c} \in \mathcal{C} \right\}, \tag{12}$$

and  $\mathcal{E}_s = \{|\mathcal{I}_s| \leq \mathbb{E}[|\mathcal{I}_s|] + n\epsilon_2\}$ . Then, conditioned on  $\mathcal{E}_1 \cap \mathcal{E}_2 \cap \mathcal{E}_s$ , the desired upper bound in (10) follows. Finally, to finish the proof, we need to bound  $\mathbb{P}((\mathcal{E}_1 \cap \mathcal{E}_2 \cap \mathcal{E}_s)^c) \leq \mathbb{P}(\mathcal{E}_1^c) + \mathbb{P}(\mathcal{E}_2^c) + \mathbb{P}(\mathcal{E}_s^c)$ .

By definition,  $\mathbb{P}(\mathcal{E}_s^c) = \mathbb{P}\{|\mathcal{I}_s| \leq \mathbb{E}[|\mathcal{I}_s|] + n\epsilon_2\}$ . Since  $|\mathcal{I}_s| = \sum_{j=1}^n \mathbb{1}_{\{y_j(D_{1,j}, \dots, D_{B,j}) > T\}} = \sum_{j=1}^n S_j$ , the variables  $S_1, \dots, S_n$  are independent Bernoulli random variables, where  $S_j = \mathbb{1}_{\{y_j(D_{1,j}, \dots, D_{B,j}) > T\}}$ . Because each  $S_j$  is bounded, Hoeffding's inequality gives

$$\mathbb{P}(|\mathcal{I}_s| \leq np_s + n\epsilon_2) \leq \exp(-2n\epsilon_2^2). \quad (13)$$

For the probabilities of  $\mathcal{E}_1$  and  $\mathcal{E}_2$ , using the union bound together with Hoeffding's inequality as in [19], we obtain  $\mathbb{P}(\mathcal{E}_1^c) + \mathbb{P}(\mathcal{E}_2^c) + \mathbb{P}(\mathcal{E}_s^c) \leq 2^{B+1} \exp(-n\epsilon_1^2/(2B^2)) + \exp(-2n\epsilon_2^2)$ .

## 4.2 Proof of Corollary 3.2

Let  $\delta' = \delta/\rho^2$ ,  $T' = T/\rho$  and  $\Delta_T = (\frac{B}{2} - T') + ((\frac{B}{2} - T')^+ + 4B)$ . Note that  $\Delta_T$  does not depend on  $p$ . Ignoring the additive noise contribution for the moment, the upper bound in Theorem 3.1 normalized by  $\rho^2$  can be written as  $g(p)$ , where

$$g(p; T) = \left(1 + \frac{Bp}{1-p}\right)\delta' + \frac{\epsilon_1}{p(1-p)} + \frac{1}{B}(p_s(\mathbf{x}; T) + \epsilon_2)\Delta_T. \quad (14)$$

Obviously minimizing  $g(p)$  is equivalent to minimizing the bound in Theorem 3.1. Note that

$$g'(p; T) = \frac{B}{(1-p)^2}\delta' + \frac{\epsilon_1(2p-1)}{p^2(1-p)^2} + \frac{\Delta_T}{B} \frac{\partial p_s(\mathbf{x}; T)}{\partial p}. \quad (15)$$

Let  $p_T^*$  denote the solution of  $g'(p; T) = 0$ . Then,

$$\epsilon_1(1-2p_T^*) = B(p_T^*)^2\delta' + \frac{\Delta_T(p_T^*)^2(1-p_T^*)^2}{B} \frac{\partial p_s(\mathbf{x}; T)}{\partial p} \Big|_{p=p_T^*}. \quad (16)$$

Recall that  $p_s(\mathbf{x}; T)$  denotes the expected number of measurements that are saturated. Therefore, increasing  $p$ , which leads to increasing the number of non-zero entries in the masks, only increases  $p_s(\mathbf{x}; T)$ . Hence,  $p_s(\mathbf{x}; T)$  is always an increasing function of  $p$ . Hence, from (16),

$$1 - 2p_T^* \geq 0,$$

To finish the proof, consider  $T_1 < T_2$  and assume that at  $T_1$  the bound is optimized at  $p_{T_1}^*$ . That is,

$$\frac{B}{(1-p_{T_1}^*)^2}\delta' + \frac{\epsilon_1(2p_{T_1}^*-1)}{(p_{T_1}^*)^2(1-p_{T_1}^*)^2} + \frac{\Delta_{T_1}}{B} \frac{\partial p_s(\mathbf{x}; T)}{\partial p} \Big|_{p=p_{T_1}^*} = 0. \quad (17)$$

Evaluating  $g'(p; T_2)$  at  $p_{T_1}^*$ , for  $T_2 > T_1$  gives

$$g'(p_{T_1}^*; T_2) = g'(p_{T_1}^*; T_1) + \frac{\Delta_{T_2} - \Delta_{T_1}}{B} \frac{\partial p_s(\mathbf{x}; T_1)}{\partial p} \Big|_{p=p_{T_1}^*} < 0, \quad (18)$$

since  $g'(p_{T_1}^*; T_1) = 0$ ,  $\Delta_{T_2} - \Delta_{T_1} < 0$ , and  $\partial p_s/\partial p \geq 0$ . Because  $g'(p; T_2)$  is strictly increasing in  $p$  on  $(0, 1/2]$  [19], the unique zero of  $g'(\cdot; T_2)$  must occur at some  $p_{T_2}^* > p_{T_1}^*$ . Hence  $p_T^*$  is strictly increasing in  $T$ , and from (16) we still have  $p_T^* < 1/2$  for all  $T$ , since the right-hand side of (16) is positive.

## 5 Experiments

We now empirically validate our analysis of SCI recovery under measurement saturation and the resulting mask optimization rules through simulations with the proposed SAPnet algorithm. The results agree with Theorem 3.1 and illustrate how saturation levels guide mask selection and influence reconstruction quality.

**Dataset and Benchmark.** We evaluate on six standard grayscale video SCI benchmarks: *Kobe*, *Runner*, *Drop*, *Traffic*, *Aerial*, and *Crash* [22], each at spatial resolution  $256 \times 256$  with  $B = 8$ . As a baseline, we use the state-of-the-art Plug-and-Play method PnP-FastDVDnet [22] and model-based method GAP-TV [23].

### 5.1 Algorithm

Solving (3) exactly is challenging due to both a non-convex objective and non-convex constraints. In the unsaturated SCI setting, PnP-FastDVDnet [22] provides a robust and efficient approximation of (2) by embedding a pretrained denoiser within an iterative scheme. A key element of this framework is the use of generalized alternating projection (GAP) [24] in place of standard gradient descent. GAP offers two advantages for SCI: (i) it requires no learning-rate tuning (we fix  $\mu = 1$ ), and (ii) it efficiently exploits the diagonal structure of the measurement operator  $\mathbf{H}$ .

Building on this framework, we introduce the *Saturation-Aware Plug-and-Play Net (SAPnet)*. Unlike standard GAP, SAPnet augments the update rule with an additional residual term that enforces consistency on saturated pixels via a thresholding operator, while retaining the PnP denoiser to impose signal structure. Algorithm 1 summarizes the resulting method.

---

**Algorithm 1** SAPnet framework for SCI recovery

---

**Require:**  $\mathbf{H}$ ,  $\mathbf{y}_T$ ; saturation level  $T$ ; stepsize  $\mu > 0$ .

- 1: Initialize  $\mathbf{x}^0 = \mathbf{0}$ .
  - 2: **for**  $t = 0$  to Max-Iter **do**
  - 3:   **Forward projection:**  $\mathbf{r}^t = \mathbf{H}\mathbf{x}^t$ .
  - 4:   **Indicator masks:**
  - 5:      $\text{unsat\_pixel} = \mathbb{1}_{\{\mathbf{y}_T < T\}}$
  - 6:      $\text{sat\_pixel} = \mathbb{1}_{\{\mathbf{y}_T = T\}}$
  - 7:   **Unsaturated:**  $\mathbf{e}_u^t = \text{unsat\_pixel} \odot (\mathbf{y}_T - \mathbf{r}^t)$ .
  - 8:   **Saturated:**  $\mathbf{e}_s^t = \text{sat\_pixel} \odot [(T - \mathbf{r}^t)_+]$ .
  - 9:   **Residual:**  $\tilde{\mathbf{e}}^t = \mathbf{e}_u^t + \mathbf{e}_s^t$ .
  - 10:   **PGD step (GAP):**  $\mathbf{s}^{t+1} = \mathbf{x}^t + \mu \mathbf{H}^\top (\mathbf{H}^\top \mathbf{H})^{-1} \tilde{\mathbf{e}}^t$ .
  - 11:   **Projection (deep denoiser):**  $\mathbf{x}^{t+1} = \mathcal{D}(\mathbf{s}^{t+1})$ .
  - 12: **end for**
  - 13: **Output:**  $\hat{\mathbf{x}} = \mathbf{x}^{\text{Max-Iter}}$ .
- 

At each iteration, unsaturated pixels are updated using the standard residual, while saturated pixels stop updating once the reconstruction reaches the threshold  $T$ . This ensures consistency with clipped measurements and avoids over-correction. Finally, note that in SCI the matrix  $\mathbf{H}^\top \mathbf{H}$  is diagonal due to the mask structure, so the inversion in line 10 reduces to simple element-wise division rather than a full matrix inversion.

### 5.2 Saturated measurements' distribution

Here we characterize how often measurements clip under realistic imaging conditions. In practice, the sensor's saturation threshold is fixed by its full-well/ADC limits, while scene illumination (radiance and exposure) varies. Because the benchmarks provide only normalized intensities, we model saturation with an effective threshold  $T$  (or normalized ratio  $T/B$ ) relative to the scene scale: decreasing  $T$  corresponds to higher effective brightness or reduced dynamic range and therefore increases the fraction of clipped samples. With this convention, varying illumination is equivalent to fixing  $\mathbf{x}$  and sweeping  $T$ , which we adopt in both

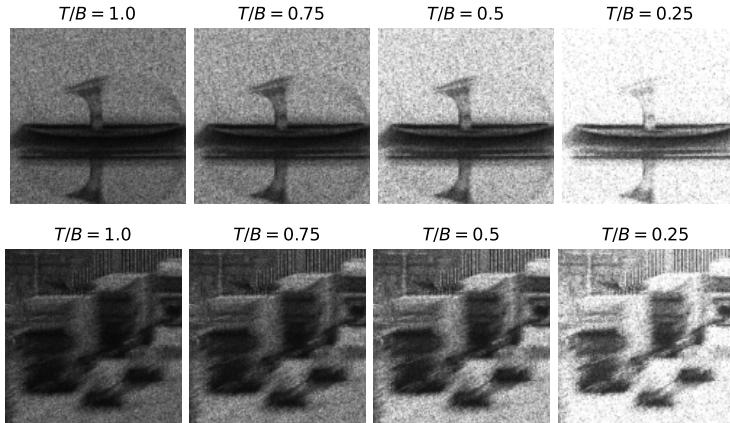


Figure 1: Measurements of Drop and Traffic under different **saturation** level of  $T$ .

analysis and simulation. Theorem 3.1 links recovery error to  $p_s(\mathbf{x}; T)$ , the expected fraction of saturated measurements. Empirically (Fig. 1–2),  $p_s(\mathbf{x}; T)$  grows as  $T$  decreases, but its rate is dataset-dependent: **Drop** and **Crash** reach  $\approx 10\%$  saturation at  $T=4$ , whereas **Kobe** remains orders of magnitude lower under the same setting. This heterogeneity explains the disparate sensitivity of reconstructions to saturation and motivates saturation-aware mask and algorithm design. Unless otherwise noted, masks in these figures are the same, entries are sampled from i.i.d.  $\text{Bern}(p = 0.5)$ .

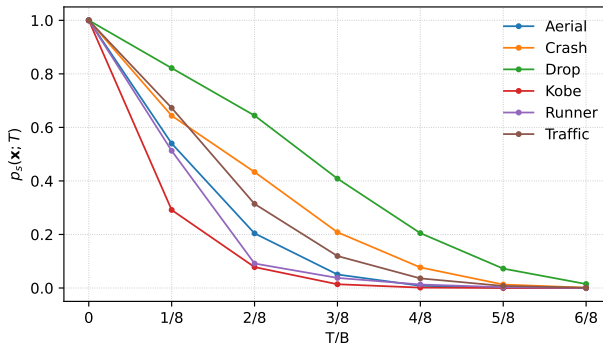


Figure 2:  $p_s(\mathbf{x}; T)$ , expected fraction of saturated measurements for different input data ( $\mathbf{x}$ ), as a function of  $T/B$ .

Table 1: PSNR improvement (dB) of SAPnet over PnP-FastDVDnet on six grayscale benchmarks under different saturation levels  $T/B$  with default masks ( $\text{Bern}(p = 0.5)$ ).

<b>Dataset</b>	$T/B = 0.25$	$T/B = 0.5$	$T/B = 0.75$
Runner	+13.148	+2.497	+0.019
Drop	+30.017	+24.677	+6.594
Crash	+11.189	+1.940	-0.028
Traffic	+6.352	+3.259	+0.072
Kobe	+6.604	+0.430	-0.009
Aerial	+4.325	+0.690	+0.017

Table 2: PSNR (dB) comparison among GAP-TV [23] (model-based), PnP-FastDVDnet [22] (pretrained deep denoiser, represent by PnP), and SAPnet (ours) on six grayscale benchmarks under different saturation levels  $T/B$  with optimized mask. **Bold** indicates the best performance and underline indicates the second-best.

Dataset	$T/B = 0.25$			$T/B = 0.5$			$T/B = 0.75$		
	GAP-TV	PnP	SAPnet	GAP-TV	PnP	SAPnet	GAP-TV	PnP	SAPnet
Runner	25.57	<u>31.88</u>	<b>37.04</b>	27.39	<u>37.01</u>	<b>37.90</b>	27.80	<u>37.92</u>	<b>37.94</b>
Drop	<u>24.76</u>	12.37	<b>42.26</b>	29.79	<u>36.29</u>	<b>43.26</b>	31.57	<u>43.03</u>	<b>43.24</b>
Crash	<u>22.25</u>	20.60	<b>26.13</b>	23.98	<u>26.25</u>	<b>26.86</b>	24.29	<b>26.87</b>	<u>26.86</u>
Traffic	18.45	<u>22.73</u>	<b>26.75</b>	19.35	<u>27.31</u>	<b>27.92</b>	19.43	<u>27.98</u>	<b>27.99</b>
Kobe	21.95	<u>28.94</u>	<b>31.70</b>	22.28	<u>32.58</u>	<b>32.75</b>	22.29	<b>32.80</b>	<u>32.79</u>
Aerial	24.33	<u>24.56</u>	<b>26.73</b>	25.42	<u>27.83</u>	<b>27.91</b>	25.54	<u>27.90</u>	<b>28.13</b>

### 5.3 SCI recovery under measurements saturation

We now report empirical results that assess SCI reconstruction in the presence of measurement saturation. We evaluate the proposed *SAPnet*, a saturation-aware Plug-and-Play algorithm that augments the standard objective with a consistency term that enforces agreement with clipped measurements. As summarized in Table 1, SAPnet delivers substantial PSNR gains over PnP-FastDVDnet on grayscale benchmarks, with average improvements of about 12 dB in strongly saturated scenarios. Beyond accuracy, SAPnet is training free and mask agnostic: it uses a fixed pretrained FastDVDnet video denoiser trained on natural images, requires no retraining across datasets, saturation levels, or mask distributions, and accommodates arbitrary binary masks by updating only the forward operator. The Plug-and-Play structure also allows the denoiser to be swapped without changing the optimization. In practice, SAPnet reconstructs a sequence of 32 frames at  $256 \times 256$  resolution in approximately 15 seconds per video and remains robust across a wide range of saturation levels and mask patterns.

To study the effect of mask distribution, we sample  $D_{ij} \stackrel{\text{iid}}{\sim} \text{Bern}(p)$  with  $p$  swept from 0.1 to 0.9 in steps of 0.1. The results in Fig. 3, obtained using Algorithm 1, show that reconstruction error is minimized for  $p^* < 0.5$ , consistent with Corollary 3.2. Moreover, the optimal  $p^*$  decreases as saturation becomes more severe, which indicates that heavier clipping benefits from sparser masks.

For comparison, we also report results of GAP-TV, a classical model-based baseline that does not explicitly model measurement saturation. As shown in Fig. 3, GAP-TV follows the same overall trend as SAPnet across datasets and mask densities, with reconstruction quality improving as saturation weakens and the mask probability approaches its optimal value, which is consistently below 0.5. As saturation increases, the optimal mask probability further decreases. However, GAP-TV consistently achieves lower PSNR than SAPnet at all saturation levels, with a larger gap in strongly saturated cases. This observation is consistent with the performance results in Table 2, and shows the benefit of explicitly enforcing saturation consistency rather than relying only on a total-variation prior.

A dataset-level analysis provides further context. As shown in Fig. 2, datasets such as *Drop* and *Crash* exhibit a larger fraction of saturated measurements and therefore suffer greater quality degradation. This sensitivity explains both the strong dependence on mask selection in Fig. 3 and the substantial gains achieved by SAPnet in Table 1.

For the setup with small measurement noise, our theoretical analysis in Section 3.1 demonstrates that the results remain robust under additive perturbations. In Fig. 4, we simulate noisy measurements with noise level  $\sigma = 10$  and compare the baseline method with the proposed SAPnet. The results show that SAPnet maintains robustness against noise, consistently achieving higher performance with optimized masks. While the optimal mask probability grows slightly compared to the ideal (noise-free) case, this behavior is consistent with the detailed explanation provided in Section 3 of [25], and corresponds to the unsaturated noisy measurement

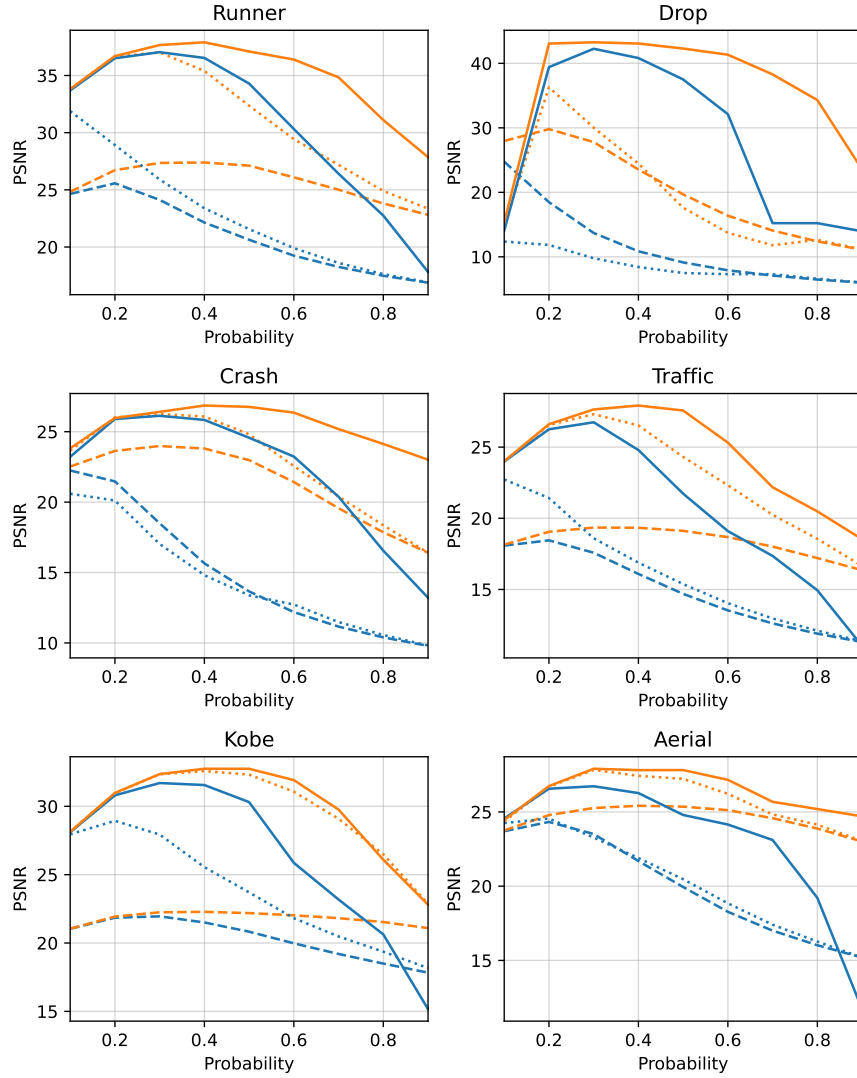


Figure 3: PSNR of  $\|\mathbf{x} - \hat{\mathbf{x}}\|$  under Bernoulli masks with i.i.d. entries  $\text{Bern}(p)$ . **Solid** lines correspond to the proposed SAPnet, **dashed** lines to GAP-TV, and **dotted** lines to PnP-FastDVDnet. **Blue** curves show results for saturation level  $T/B = 0.25$ , while **orange** curves show results for  $T/B = 0.5$ .

results.

In summary, the experiments show that SAPnet consistently improves reconstruction under clipping, with average gains of approximately 12 dB at  $T/B = 0.25$  and 5.6 dB at  $T/B = 0.5$ , while maintaining efficient per-video runtime. The optimal Bernoulli mask density lies below 0.5 and decreases as saturation strengthens, and datasets with larger saturation probability  $p_s(\mathbf{x}; T)$  benefit the most. These findings provide practical guidance for choosing masks and reconstruction settings in saturated SCI.

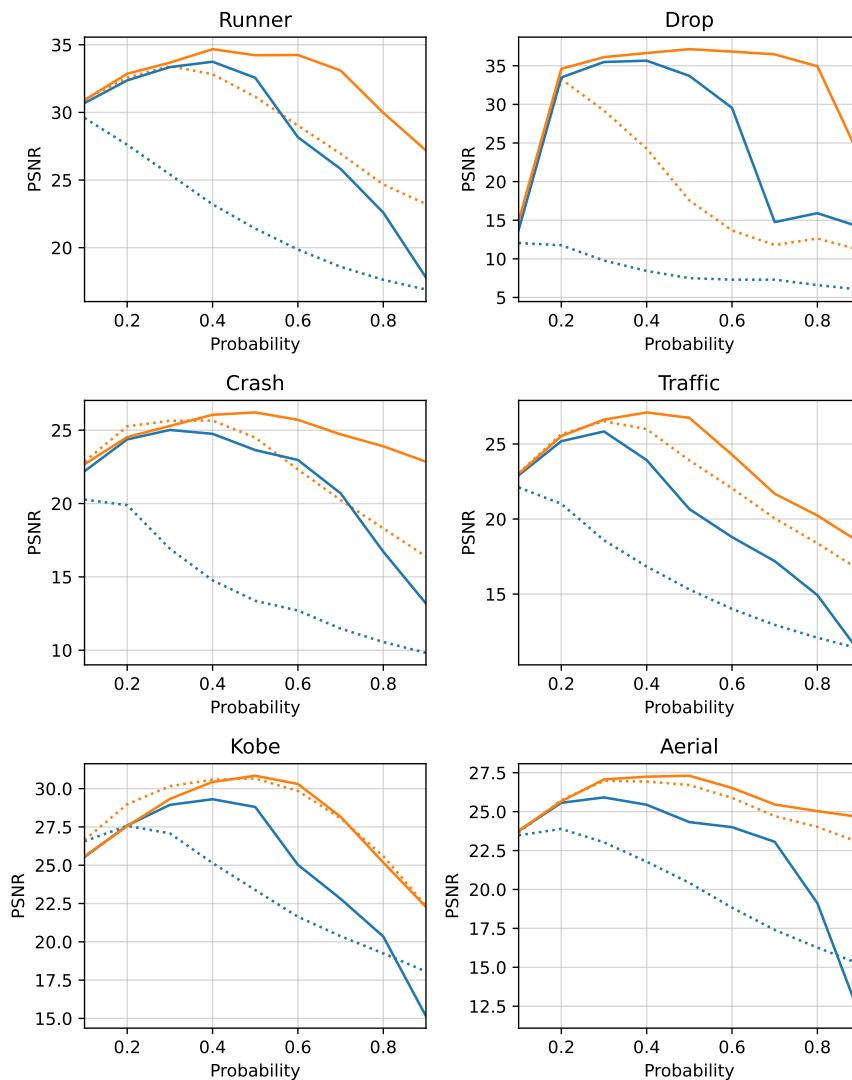


Figure 4: **Noisy measurement** recover of PSNR of  $\|\mathbf{x} - \hat{\mathbf{x}}\|$  under different masks with elements that are i.i.d.  $\text{Bern}(p)$ . **Solid** lines represent results obtained with the proposed SAPnet, while **dotted** lines correspond to PnP-FastDVDnet. **Blue** curves indicate a saturation threshold of  $T/B = 0.25$ , and **Orange** curves indicate  $T/B = 0.5$ .

## 6 Conclusion

In this paper, we presented the first systematic analysis of SCI systems under measurement saturation. Our theoretical results establish that binary masks with Bernoulli distribution achieve optimal recovery when the probability of ones ( $p$ ) is below 0.5, and that stronger saturation requires even smaller  $p$ . These insights provide a principled guideline for mask design in practice. Complementing the theory, we proposed SAPnet, a saturation-aware plug-and-play reconstruction algorithm that introduces a consistency loss term to explicitly account for clipped measurements. Experiments on standard video SCI benchmarks validate the theory and demonstrate substantial PSNR improvements over PnP-FastDVDnet, while maintaining low computational cost and robustness across saturation levels and mask patterns.

## References

- [1] P. Llull, X. Liao, X. Yuan, J. Yang, D. Kittle, L. Carin, G. Sapiro, and D. J. Brady, “Coded aperture compressive temporal imaging,” *Opt. Exp.*, vol. 21, no. 9, pp. 10526–10545, 2013.
- [2] M. Gehm, R. John, D. Brady, R. Willett, and T. Schulz, “Single-shot compressive spectral imaging with a dual-disperser architecture,” *Optics express*, vol. 15, no. 21, pp. 14013–14027, 2007.
- [3] A. Wagadarikar, R. John, R. Willett, and D. J. Brady, “Single disperser design for coded aperture snapshot spectral imaging,” *App. Optics*, pp. B44–B51, 2008.
- [4] X. Yuan, D. J. Brady, and A. K. Katsaggelos, “Snapshot compressive imaging: Theory, algorithms, and applications,” *IEEE Sig. Proc. Mag.*, 2021.
- [5] J. Laska, P. Boufounos, M. Davenport, and R. Baraniuk, “Democracy in action quantization, saturation, and compressive sensing,” *Applied and Computational Harmonic Analysis*, vol. 31, no. 3, pp. 429–443, 2011.
- [6] L. Rencker, F. Bach, W. Wang, and M. Plumbley, “Sparse recovery and dictionary learning from nonlinear compressive measurements,” *IEEE Transactions on Signal Processing*, vol. 67, no. 21, pp. 5659–5670, 2019.
- [7] S. Foucart and J. Li, “Sparse recovery from inaccurate saturated measurements,” *Acta Applicandae Mathematicae*, vol. 158, no. 1, pp. 49–66, 2018.
- [8] S. Banerjee, Sudhansh Peddabomma, Radhendushka Srivastava, and Ajit Rajwade, “A likelihood based method for compressive signal recovery under gaussian and saturation noise,” *Signal Processing*, p. 109349, 2024.
- [9] P. Wang, L. Wang, and X. Yuan, “Deep optics for video snapshot compressive imaging,” in *Proceedings of the IEEE/CVF International Conference on Computer Vision (ICCV)*, October 2023, pp. 10646–10656.
- [10] B. Zhang, X. Yuan, C. Deng, Z. Zhang, J. Suo, and Q. Dai, “End-to-end snapshot compressed super-resolution imaging with deep optics,” *Optica*, Apr 2022.
- [11] C. Metzler, H. Ikoma, Y. Peng, and G. Wetzstein, “Deep optics for single-shot high-dynamic-range imaging,” in *Proceedings of the IEEE/CVF Conference on Computer Vision and Pattern Recognition (CVPR)*, June 2020.
- [12] J. Martel, L. Müller, S. Carey, P. Dudek, and G. Wetzstein, “Neural sensors: Learning pixel exposures for hdr imaging and video compressive sensing with programmable sensors,” *IEEE Transactions on Pattern Analysis and Machine Intelligence*, 2020.
- [13] Y. Cai, X. Liu, Z. Wang, X. Liu, W. Li, G. Wang, T. Li, and X. Yuan, “The extreme performance of video snapshot compressive imaging under system noise constraints,” *Optics & Laser Technology*, vol. 192, pp. 113913, 2025.
- [14] Y. Zhao and E. Lam, “Sasa: saliency-aware self-adaptive snapshot compressive imaging,” in *ICASSP 2024-2024 IEEE International Conference on Acoustics, Speech and Signal Processing (ICASSP)*. IEEE, 2024.
- [15] H. Zhang, Q. Ye, K. Sun, Y. Li, Y. Wu, H. Xu, and H. Luo, “Anti-laser interference methods for compressive spectral imaging based on grayscale coded aperture,” *Optics Continuum*, vol. 3, no. 1, pp. 102–111, 2024.
- [16] C. Correa, H. Arguello, and G. Arce, “Spatiotemporal blue noise coded aperture design for multi-shot compressive spectral imaging,” *Journal of the Optical Society of America A*, vol. 33, no. 12, pp. 2312–2322, 2016.

- [17] N. Diaz, C. Hinojosa, and H. Arguello, “Adaptive grayscale compressive spectral imaging using optimal blue noise coding patterns,” *Optics & Laser Technology*, vol. 117, pp. 147–157, 2019.
- [18] S. Jalali and X. Yuan, “Snapshot compressed sensing: Performance bounds and algorithms,” *IEEE Trans. Inform. Theory*, vol. 65, no. 12, pp. 8005–8024, 2019.
- [19] M. Zhao and S. Jalali, “Theoretical characterization of effect of masks in snapshot compressive imaging,” *SIAM Journal on Imaging Sciences*, vol. 18, no. 3, pp. 1707–1741, 2025.
- [20] M. Zhao and S. Jalali, “Saturation-aware snapshot compressive imaging: theory and algorithm,” *arXiv preprint arXiv:2501.11869*, 2025.
- [21] M. Zhao and S. Jalali, “Theoretical analysis of binary masks in snapshot compressive imaging systems,” in *2023 59th Annual Allerton Conf. on Comm., Cont., and Comp. (Allerton)*. IEEE, 2023, pp. 1–8.
- [22] X. Yuan, Y. Liu, J. Suo, F. Durand, and Q. Dai, “Plug-and-play algorithms for video snapshot compressive imaging,” *IEEE Trans. Pattern Anal. Mach. Intell.*, vol. 44, no. 10, pp. 7093–7111, 2021.
- [23] X. Yuan, “Generalized alternating projection based total variation minimization for compressive sensing,” in *IEEE Int. Conf. on Image Proc. (ICIP)*. IEEE, 2016, pp. 2539–2543.
- [24] X. Liao, H. Li, and L. Carin, “Generalized alternating projection for weighted-2,1 minimization with applications to model-based compressive sensing,” *SIAM Journal on Imaging Sciences*, vol. 7, no. 2, pp. 797–823, 2014.
- [25] Mengyu Zhao, Xi Chen, Xin Yuan, and Shirin Jalali, “Untrained neural nets for snapshot compressive imaging: Theory and algorithms,” in *The Thirty-eighth Annual Conference on Neural Information Processing Systems*, 2024.